

1 **Response of Coastal California Hydroclimate to the Paleocene-** 2 **Eocene Thermal Maximum**

3 Xiaodong Zhang^{1*}, Brett J. Tipple², Jiang Zhu³, William D. Rush⁴, Christian A. Shields³, Joseph
4 B. Novak⁵, James C. Zachos¹

5 ¹Department of Earth and Planetary Sciences, University of California, Santa Cruz, CA 95064, USA

6 ²FloraTrace Inc., Salt Lake City, UT 84103, USA

7 ³Climate and Global Dynamics Laboratory, National Center for Atmospheric Research, Boulder, CO 80307, USA

8 ⁴Department of Environmental Studies and Sciences, Santa Clara University, Santa Clara, CA 95053, USA

9 ⁵Department of Ocean Sciences, University of California, Santa Cruz, CA 95064, USA

10 *Correspondence to: Xiaodong Zhang (xzhan335@ucsc.edu)

11 **Abstract.** The effects of anthropogenic warming on the hydroclimate of California are becoming
12 more pronounced, with increased frequency of multi-year droughts and flooding. As a past
13 analog for the future, the Paleocene-Eocene Thermal Maximum (PETM) is a unique natural
14 experiment for assessing global and regional hydroclimate sensitivity to greenhouse gas
15 warming. Globally, extensive evidence (i.e., observations, climate models with high $p\text{CO}_2$)
16 demonstrates hydrological intensification with significant variability from region to region (i.e.,
17 dryer or wetter, or greater frequency and/or intensity of extreme events). Central California
18 (paleolatitude $\sim 42^\circ\text{N}$), roughly at the boundary between dry subtropical highs and mid-latitude
19 low pressure systems, would have been particularly susceptible to shifts in atmospheric
20 circulation and precipitation patterns/intensity. Here, we present new observations and climate
21 model output on regional/local hydroclimate responses in central California during the PETM.
22 Our findings based on multi-proxy evidence within the context of model outputs suggest a
23 transition to an overall drier climate punctuated by increased precipitation during summer
24 months along the central coastal California during the PETM.

25 **1 Introduction**

26 Global warming of a few degrees celsius over the next century is projected to intensify the
27 hydrological cycle on a range of temporal and spatial scales, manifested primarily by amplified
28 wet-dry cycles (Held and Soden, 2006; Douville et al., 2021). Indeed, just over last few decades
29 there has been an increasing frequency in the severity of extremes characterized by compound
30 heat waves and intense drought (Büntgen et al., 2021; Williams et al., 2020; Zscheischler and
31 Lehner, 2022), and/or heavy precipitation and flooding (Liu et al., 2020; Risser and Wehner,
32 2017). As greenhouse gas driven warming continues, such precipitation extremes (wet or dry)
33 are expected to intensify (Stevenson et al., 2022). This is particularly so for California which
34 receives much of its rainfall from winter systems fueled by atmospheric rivers (AR), the
35 frequency of which are forecast to decline as the systems shift northward (Simon Wang et al.,
36 2017). The decline in winter precipitation along with warming will create more intense droughts
37 even as the potential for extreme precipitation events increases (Vogel et al., 2020; Swain et al.,
38 2018).

39 Climate model predictions for intensification of the hydrological cycle are supported by case
40 studies of extreme warming events of the deep past (Carmichael et al., 2017). In particular, the
41 Paleocene-Eocene Thermal Maximum (PETM) has emerged as a unique natural experiment for
42 assessing global and regional hydroclimate sensitivity to greenhouse gas warming (Zachos et al.,
43 2008). Extensive evidence exists for a major mode shift of local/regional precipitation patterns
44 and intensity (Pagani et al., 2006; Slotnick et al., 2012; Schmitz and Pujalte, 2003; Sluijs and
45 Brinkhuis, 2009; Smith et al., 2007; Handley et al., 2012; Kozdon et al., 2020) including
46 enhanced erosion and extreme flooding in fluvial sections (e.g., Pyrenees; Bighorn basin), and
47 increased weathering and sediment fluxes to coastal basins (e.g., Bass River, Wilson Lake, mid-
48 Atlantic coast; Mead Stream, New Zealand etc.) along with other observations (John et al., 2008;
49 Nicolo et al., 2010; Stassen et al., 2012; Self-Trail et al., 2017; Wing et al., 2005; Kraus and
50 Riggins, 2007; Foreman, 2014).

51 These observations of regional hydroclimate serve as the basis for climate model experiments
52 forced with proxy-based estimates of $\Delta p\text{CO}_2$ for the PETM (i.e., 3x-6x pre-industrial)(Kiehl and
53 Shields, 2013; Carmichael et al., 2016; Zhu et al., 2020). Using such estimates, model
54 simulations show an overall increase in poleward meridional water vapor transport as manifested
55 by a net increase in evaporation of subtropical regions, balanced by higher precipitation of

56 tropical/high latitudes characterizing the ‘wet-gets-wetter and dry-gets-drier’ hydrological
57 response. The latest simulations using high-resolution climate models display several key
58 regional responses including increased frequency of extreme precipitation events, especially the
59 coastal regions where atmospheric rivers (AR) are common (Rush et al., 2021). Indeed,
60 observations of high-energy flooding events in SW Europe (i.e., the Pyrenees) during the PETM
61 (Schmitz and Pujalte, 2003) can be explained by increased frequency of North Atlantic ARs
62 contributing landfall in that region. Pacific AR activity as simulated for the PETM also becomes
63 more intense but less frequent along the central California coast by shifting northward with the
64 storm tracks (Shields et al., 2021), not unlike the projections for California in the future (Shields
65 and Kiehl, 2016; Massoud et al., 2019). This pattern is consistent with warming scenarios in
66 general which have weakened zonal wind belts (i.e., the westerlies) that are shifting poleward
67 (Abell et al., 2021; Douville et al., 2021).

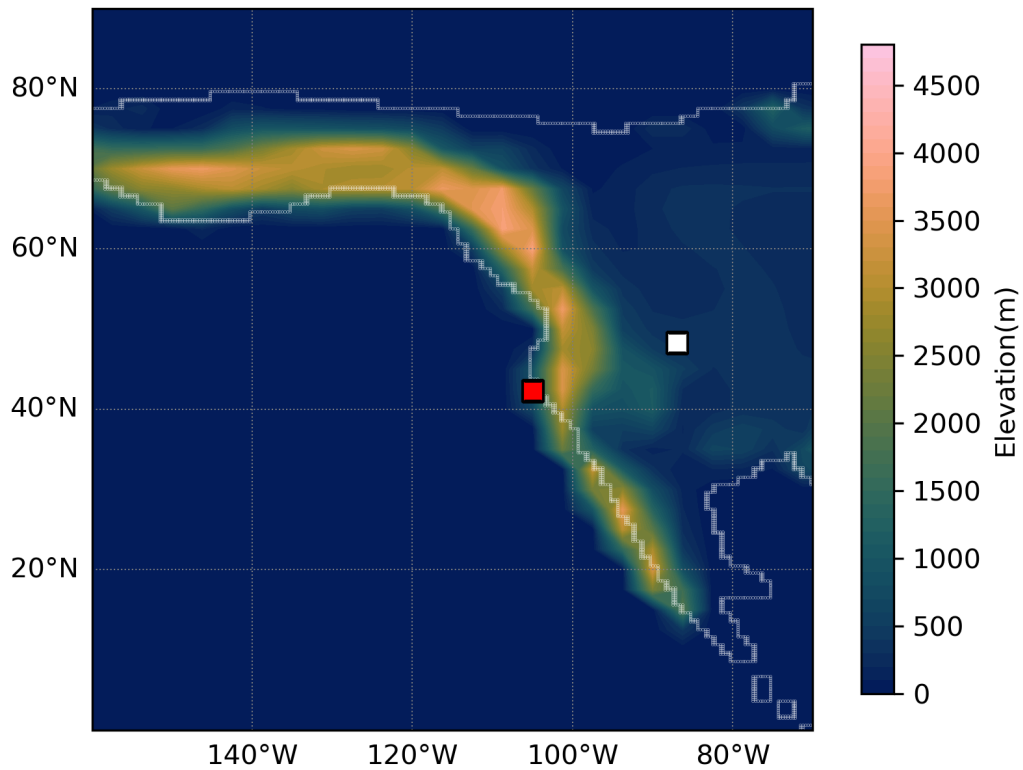
68 Testing the theoretical response of extreme global warming on Pacific ARs and impacts on
69 seasonal precipitation along North America’s western coast in general is challenging and still
70 limited by the lack of observations. Here we constrain the regional hydroclimate response along
71 the central California coast during the PETM using several independent proxies (i.e., clay
72 mineralogy, grain size distribution, $\delta^{13}\text{C}_{\text{org}}$ stratigraphy, and leaf wax $\delta^2\text{H}_{n\text{-alkane}}$ isotope records),
73 which are either directly or indirectly sensitive to shifts in precipitation patterns/intensity. These
74 proxies are then compared against Earth System model simulations of the greenhouse gas forced
75 changes in regional precipitation (i.e., pattern/intensity). The new records complement data from
76 a previous study (John et al., 2008), and along with the latest climate modeling experiments
77 provide a unique case study of the sensitivity of regional hydroclimate to major greenhouse
78 warming.

79 **2 Materials and methods**

80 **2.1 Site Location**

81 The studied outcrop section is part of the late Paleocene-early Eocene Lodo Formation located in
82 the Panoche Hill of central California (Fig. 1). During the late Paleocene, the section was
83 situated at a paleolatitude $\sim 42^\circ\text{N}$, roughly at the boundary between the dry subtropical highs and
84 mid-latitude low-pressure systems. The Lodo Formation is comprised primarily of siltstone with

85 a relatively low abundance of calcareous microfossils truncated by thin glauconitic sand layers
86 (Brabb, 1983). Depositional facies are consistent with neritic-bathyal setting along the outer shelf
87 (John et al., 2008).



88
89 Figure 1. Paleogeography and location of the Lodo Gulch section (red spot) along the Pacific
90 coast and Big Horn Basin (white spot) in the North America continent for reference at 56 Ma.
91 Late Paleocene-early Eocene topography boundary of North America was adapted from Lunt et
92 al. (2017).

93

94 2.2 Methods

95 2.2.1 Bulk organic stable carbon isotopes

96 Sediment samples used for this study include those originally collected (ca. 28) by John et al.
97 (2008). In addition, new samples (ca. 27) were collected from the upper Paleocene for organic C

98 isotopic analyses ($\delta^{13}\text{C}_{\text{org}}$) to better establish pre-PETM baseline. Samples were analyzed in the
99 UCSC Stable Isotope Laboratory using a CE instruments NC2500 elemental analyzer coupled
100 with Thermo Scientific Delta Plus XP iRMS via a Thermo-Scientific ConFlo III. All samples
101 were calibrated with VPDB (Vienna PeeDee Belemnite) for $\delta^{13}\text{C}$ and AIR for $\delta^{15}\text{N}$ against an in-
102 house gelatin standard reference material (PUGel). Analytical reproducibility precision is \pm
103 0.1 ‰ for $\delta^{13}\text{C}$ and ± 0.2 ‰ for $\delta^{15}\text{N}$.

104 2.2.2 Grain Size analyses

105 Particle size was measured by laser diffraction using Beckman Coulter with Polarization
106 Intensity Differential Scatter (PIDS) housed at UCSC (see supplemental information). For each
107 sample, 2 to 5 mg of bulk sediment was powdered and sieved through a 2-mm sieve following
108 the protocols in Blott et al., (2004). A total of 39 samples were measured, each in duplicate or
109 triplicate to ensure reproducibility.

110 2.2.3 Clay Assemblages analyses

111 Sample preparation followed a slightly modified version of Kemp et al., (2016). Roughly 5 to 10
112 g of sediment was powdered in a pestle and mortar and then placed in a Calgon (Sodium
113 hexametaphosphate) solution on a shaker table for 72 hours. Samples were sorted through a 63
114 μm sieve while collecting the fluid with the <63 μm fraction. The collected fluid and suspended
115 fine fraction (< 63 μm) were allowed to settle for a period determined by Stokes' Law to keep $<$
116 $2\mu\text{m}$ size clay particles remaining in suspension. The fluid was then decanted and dried in the
117 oven at 40°C . Approximately 150 mg clay of each sample were used to prepared oriented mounts
118 for X-ray diffraction (XRD) analysis. A total of 38 clay samples were prepared from the Lodo
119 Formation. The sample residues were measured on a Philips 3040/60 X'pert Pro X-ray
120 diffraction instrument at UCSC. Clay species (i.e., Smectite, Illite, Kaolinite, Chlorite) were
121 identified based on peak positions and intensities representing each clay mineral.

122 2.2.4 Leaf wax distribution and carbon/hydrogen isotopic composition

123 Sediment extraction, compound isolation, and compound-specific isotope measurements were
124 conducted following Tipple et al., (2011). Briefly, sediments were freeze-dried, powdered (~ 500
125 g), and extracted with dichloromethane (DCM): methanol (2:1, v/v) using a Soxhlet extractor.

126 Total lipid extracts were concentrated and then separated by column chromatography using silica
127 gel. *N*-alkanes were further purified from cyclic and branched alkanes using urea adduction
128 following Wakeham and Pease, (2004). *N*-alkane abundances were determined using gas
129 chromatograph (GC) with a flame ionization detector (FID). Isotope analyses were then
130 performed using a GC coupled to an iRMS interfaced with a GC-C III combustion system or a
131 High Temperature Conversion system for $\delta^{13}\text{C}$ and $\delta^2\text{H}$ analyses, respectively. 59 samples were
132 processed with a fused silica, DB-5 phase column (30 m \times 0.25 mm I.D., 0.25 μm film
133 thickness) with helium as the carrier at a flow of 1.5ml/min. GC oven temperature program was
134 60-320°C @ 5°C/min and isothermal for 30 min. A Thermo Trace MS was used for detection
135 with the mass spec scanning from 50-800 m/z or exclusively m/z of 191, 217, 218, 370, 372,
136 386, and 400 for single ion monitoring. Biomarkers were identified by elution time and mass
137 spectra of in-house petroleum standards with published biomarker distributions (Peters et al.,
138 2005).

139 $\delta^{13}\text{C}$ and $\delta^2\text{H}$ values are expressed relative to Vienna Pee Dee belemnite (VPDB) and Vienna
140 Standard Mean Ocean Water (VSMOW). Individual *n*-alkane isotope ratios were corrected to *n*-
141 alkane reference materials (for $\delta^{13}\text{C}$, C₂₀, C₂₅, C₂₇, C₃₀, and C₃₈ of known isotopic ratio and for
142 $\delta^2\text{H}$, “Mix A” from Arndt Schimmelmann, Indiana University) analyzed daily at several
143 concentrations. In addition, H₂ reference gas of known isotopic composition was pulsed between
144 sample *n*-alkane peaks to confirm if normalizations were appropriate. Standard deviations (SD)
145 of *n*-alkane reference materials were $\pm 0.6\text{‰}$ for $\delta^{13}\text{C}$ and $\pm 6\text{‰}$ for $\delta^2\text{H}$.

146 2.2.5 Earth System/Climate Models

147 Climate simulations from two models were used in this paper for (1) comparison with leaf wax
148 proxy data and (2) extreme events analyses. (1) Water isotope-enabled Community Earth System
149 Model version 1.2 (iCESM1.2) simulates changes in climate and water isotopic composition
150 during the PETM (Zhu et al., 2020) with a horizontal resolution of 1.9 \times 2.5° in atmosphere and
151 land, and a nominal 1 degree in the ocean and sea ice components. Water isotope capabilities
152 have been incorporated into all the components of CESM 1.2 (Brady et al., 2019), which include
153 the Community Atmosphere Model, version 5 (CAM5) for the atmosphere, the Parallel Ocean
154 Program, version 2 (POP2) for the ocean, the Community Land Model, version 4 (CLM4) for the
155 land, River Transport Model (RTM) for river flow, and Community Ice Code, version 4 for sea

156 ice. All simulations were run with the identical boundary conditions (including early Eocene
157 paleogeography, land-sea mask, vegetation distribution, and pre-industrial (PI) non-CO₂
158 greenhouse gas concentrations, soil properties, natural aerosol emissions, solar constant and
159 orbital parameters) following the DeepMIP protocol (Lunt et al., 2017) and differ only in
160 atmospheric CO₂ concentration. Crucially, the models with reduced latitudinal temperature
161 gradients (e.g., GFDL, CESM) more closely reproduce proxy-derived precipitation estimates and
162 other key climate metrics (Cramwinckel et al., 2022). Increased climate sensitivity with warming
163 and cloud feedback in CESM1.2 over earlier models improved water vapor sensitivity. (2) Using
164 the same CESM1.2 framework, high resolution (0.25°) simulations were conducted with forced
165 sea surface temperatures (SSTs) and active atmosphere and land components (CAM5, CLM4).
166 RTM was run at 1° resolution, and forced SST were calculated from consistent 2° fully coupled
167 PETM simulations (see details in Rush et al., 2021 and reference therein). The much higher
168 horizontal resolution in the atmosphere enables improved simulation of the extreme events.
169 Hourly, daily (CAM5), and monthly (iCESM1.2) temporal resolution precipitation outputs from
170 both sets of climate simulations were utilized in this paper, with 100 years taken from the
171 equilibrated iCESM1.2 simulations, and 15 years from the forced SST high resolution CAM5
172 simulations.

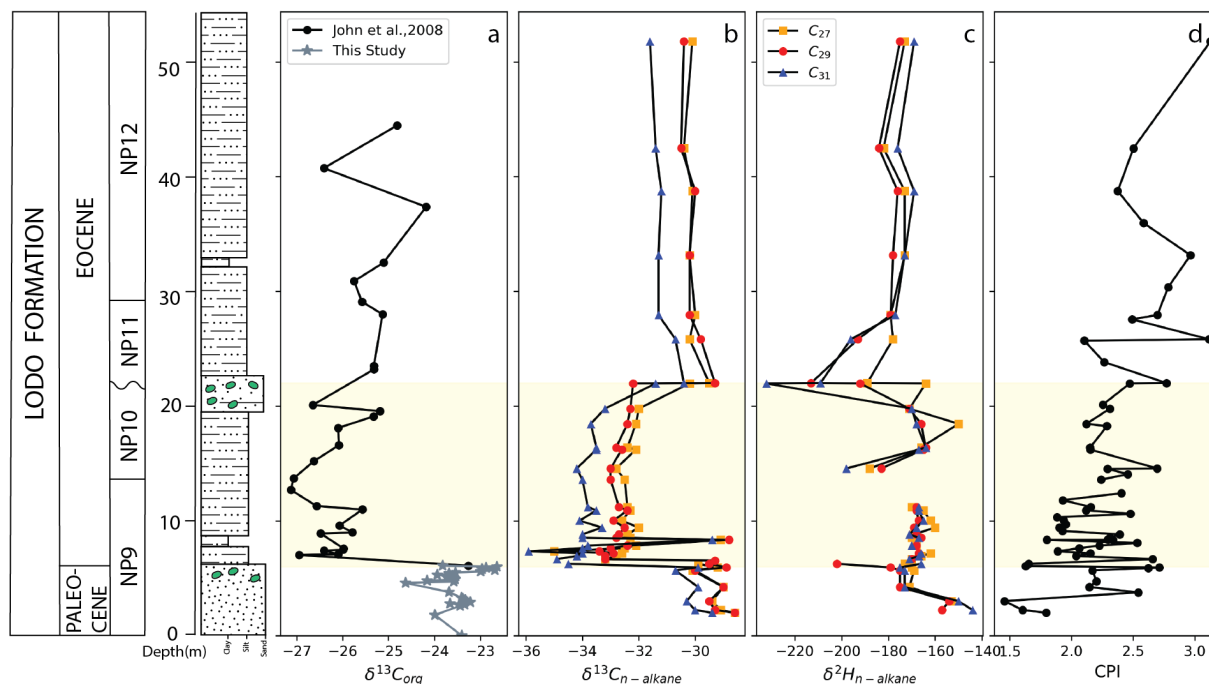
173

174 **3 Results**

175 3.1 Bulk organic and *n*-alkane stable carbon isotopes

176 A carbon isotope excursion is present in both bulk organic (Fig. 2a) and carbonate based $\delta^{13}\text{C}$
177 records (John et al., 2008) across the P-E boundary, marking the PETM onset of the Lodo
178 section. The terrestrial leaf wax *n*-alkane records all capture the carbon isotope excursion (CIE)
179 with a pattern that roughly parallels the other published records (i.e., planktonic foraminifera)
180 (John et al 2008), though is much less noisy than the bulk $\delta^{13}\text{C}_{\text{org}}$ record, not unexpected given
181 the potentially variable composition of the bulk organic matter. The magnitude of the $\Delta\delta^{13}\text{C}_{n-}$
182 *alkane* is roughly -4‰ (average of n-C₂₇, n-C₂₉, n-C₃₁) at the onset of the CIE, followed by a
183 gradual recovery that is truncated at the disconformity between 20.3m and 23.5m (coincides with
184 nanofossil biozone boundary NP10 and NP11), thus marking the top of the PETM body (Fig.
185 2a). The disconformity coincides with a global sea level regression (John et al., 2008). Following

186 the recovery, above the disconformity, the mean $\delta^{13}\text{C}_{n\text{-alkane}}$ is depleted relative to the pre-PETM
 187 baseline as is observed in most other PETM sections (Tippie et al., 2011; Handley et al., 2012).



188
 189 Figure 2. Terrestrial higher plant leaf wax n -alkane $\delta^{13}\text{C}$ and $\delta^2\text{H}$ records. The shaded area
 190 represents the bounds of the CIE/PETM (a) bulk organic carbon isotope record of Lodo Fm. (b,c)
 191 leaf wax compound specific carbon/hydrogen isotope records in $n\text{-C}_{27}$ (yellow square), $n\text{-C}_{29}$ (red
 192 closed circle), $n\text{-C}_{31}$ (blue triangle), (d) n -alkane carbon preference indices (CPI).

193
 194 3.2 Hydrogen isotopes
 195 The leaf wax $\delta^2\text{H}_{n\text{-alkane}}$ values range from -150 to -213‰ over the entire sampled section has an
 196 initial decrease of 25‰ (from -150 to -175‰ in C_{29}) just prior to the CIE onset and then
 197 followed by a slight rise (~ 6 ‰) right after the onset. The relatively invariable $\delta^2\text{H}_{n\text{-alkane}}$ through
 198 the PETM is punctuated with two brief intervals of more negative values (-202‰ at 6.26m and -
 199 213‰ at 22m). The second larger anomaly coincides with the disconformity (related to local sea
 200 level regression). The post-PETM $\delta^2\text{H}_{n\text{-alkane}}$ values are on average lower than for the upper
 201 Paleocene/PETM. Given the limited number of samples to establish a baseline for the upper
 202 Paleocene, the significance of the pre (and post CIE) shifts/anomalies in $\delta^2\text{H}_{n\text{-alkane}}$ should be
 203 considered with some caution. Several other sections do show pre-CIE shifts, both positive and

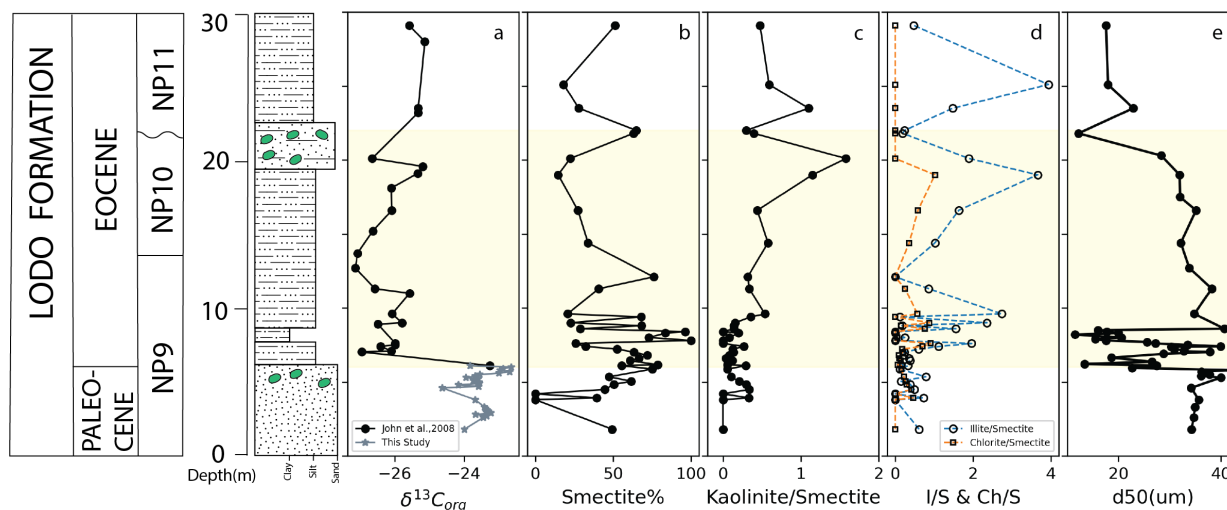
204 negative, and typically an enrichment with the CIE (Handley et al., 2008, 2011; Jaramillo et al.,
 205 2010; Tipple et al., 2011). Such minor changes likely reflect unconstrained orbital influences on
 206 regional precipitation (Rush et al., 2022; Campbell et al., 2024), especially considering the
 207 variable direction of change from location to location.

208

209 3.3 Clay assemblage and grain size

210 Clay assemblages and particle grain size should to some extent be influenced by regional
 211 hydroclimate. At Lodo, the clay assemblages (Fig. 3) are dominated by smectite throughout. The
 212 minor clay components illite and chlorite show several spikes relative to smectite within the
 213 lower (8 to 10 m) and upper CIE (~19 m), whereas the ratio of kaolinite gradually increases (0.5
 214 to 1.5) only over the upper portion of the CIE (10 to 20 m). A delayed rise in kaolinite has also
 215 been observed in a few other PETM sections whereas some show an immediate rise (Tateo,
 216 2020; Gibson et al., 2000). The smectite concentration and kaolinite/smectite ratio remain high in
 217 the post-PETM interval. The late Paleocene of Lodo Formation, with relative coarse sandy size,
 218 shows slight spikes of kaolinite associated with other minerals. Grain size, largely silt and clay,
 219 shows a distinct shift toward finer fractions (i.e., clay) with the onset of the CIE (Fig. 3e).

220



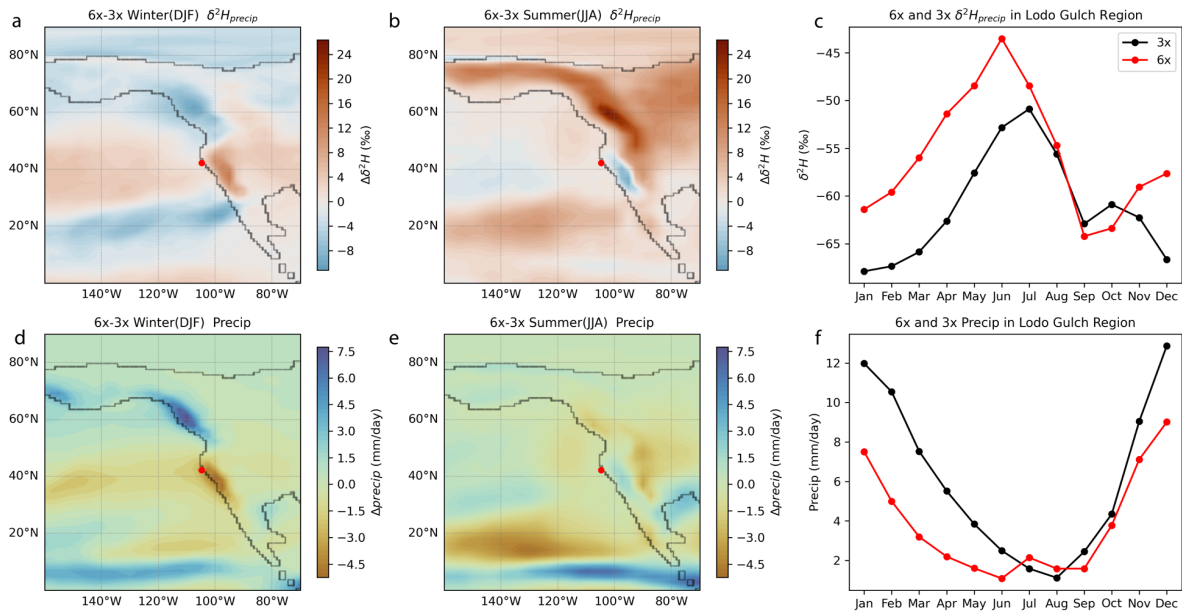
221

222 Figure 3. Integrated C isotope and clay assemblage records of Lodo Fm in the Lodo Gulch of
 223 central California (a) bulk organic carbon isotope, (b,c,d,e) clay assemblage ratios, (e) decreasing
 224 mean particle size (D50: 50% of the total particle size in sediments) corresponds to CIE onset.

225

226 3.4 Earth system model simulations

227 We obtained and processed temperature and precipitation output from two community earth
 228 system/climate models: the isotope-enabled iCESM1.2 and high-resolution CAM5 models (daily
 229 precipitation over 15 years) forced by a range of greenhouse conditions (1x,3x,6x,9x $p\text{CO}_2$ pre-
 230 industrial), both with Eocene paleogeography. For comparisons with observations, we used
 231 output from the 3x to 6x $p\text{CO}_2$ simulations which best replicated the observed SST (ΔSST) for
 232 the pre-PETM and PETM (Zhu et al., 2020). Overall, monthly winter precipitation for the study
 233 region decreases ($\sim 30\%$) during the PETM in both simulations with a slight increase in the
 234 summer (Fig. 4,5). CAM5 output shows a modest decrease in mean annual precipitation with
 235 significant seasonal shifts during the PETM (Fig. 5a). Seasonal changes of monthly averaged
 236 $\delta^{18}\text{O}$ and $\delta^2\text{H}$ from mean monthly precipitation in iCESM1.2 of central California are consistent
 237 with CAM5. On average the $\delta^2\text{H}_{\text{precip}}$ increases by ca. 5-10 ‰ from pre-PETM to PETM,
 238 especially in the winter/spring, with a smaller shift in summer/fall (1~2 ‰) (Fig 4. a,b,c). The
 239 Extreme value index (ξ), a representation of the distribution of exceedance right tail
 240 (supplemental information), shows a small but statistically robust increase in wet extremes of
 241 winter (DJF) with a significant increase in summer (JJA) wet exceedances during the PETM in
 242 the precipitation output from CAM5 simulations (Fig. 5b).

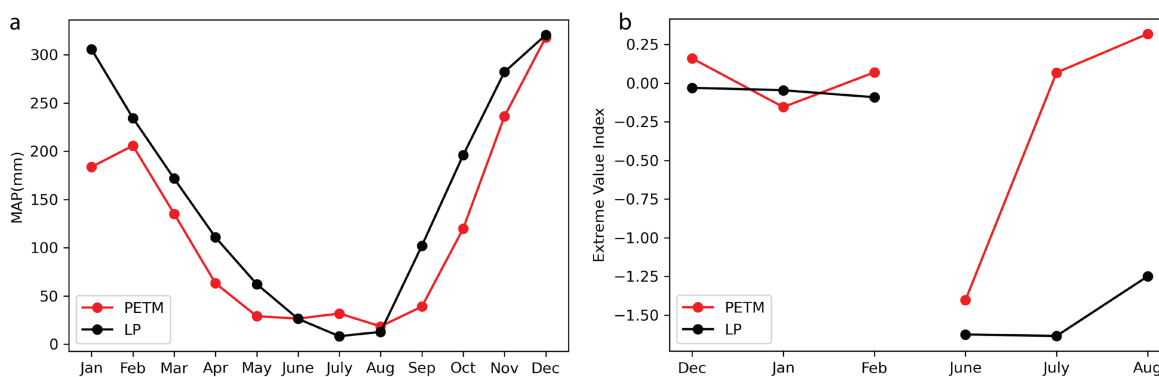


243

244 Figure 4. Seasonal and monthly meteoric precipitation amounts (mm/day) and H-isotopic
 245 composition for the North Pacific/Western N. America as simulated with the iCESM1.2 (Zhu et

246 al., 2020) under pre-PETM (3x in black) and PETM (6x in red) $p\text{CO}_2$ forcing. Panels (a) and (b)
 247 show $\Delta\delta^2\text{H}_{\text{precip}}$ between pre-PETM (3x) and PETM (6x) in winter (DJF) and summer (JJA).
 248 Panel (c) shows the annual seasonal cycle of $\delta^2\text{H}_{\text{precip}}$ at Lodo Gulch (pre-PETM in black, PETM
 249 in red). Mean daily precipitation rate difference for (d) winter and (e) summer between pre-
 250 PETM (3x) and PETM (6x). Panel (f) shows the annual seasonal cycle of daily precipitation rate
 251 at Lodo Gulch. Values represent the area-weighted average over $4^\circ \times 4^\circ$ box bounding the study
 252 site.

253



254

255 Figure 5. High resolution CAM5 model output (Shields et al., 2021) of (a) mean monthly
 256 precipitation at Lodo over 15 model years for the Late Paleocene/LP under low $p\text{CO}_2$ (680
 257 ppmv) and for the PETM under high $p\text{CO}_2$ (1590ppmv). (b) Extreme value index (ξ) comparison
 258 of mean monthly precipitation in winter and summer of central coastal California region.

259

260 4 Discussion

261 4.1 Hydroclimate response from model simulations.

262 In all model simulations of the PETM forced with higher $p\text{CO}_2$ (e.g., 3x to 6x pre-industrial), the
 263 hydrological cycle intensifies as manifested by increases in global mean precipitation and
 264 meridional vapor transport (Kiehl and Shields, 2013; Kiehl et al., 2018; Carmichael et al., 2016;
 265 Zhu et al., 2020). Regionally however, the magnitude and even the sign of precipitation change
 266 can differ considerably from global means (Carmichael et al., 2016, 2017). This is most evident
 267 in the latest low and high-resolution model simulations of the PETM (Zhu et al, 2020; Shields et
 268 al., 2021). For central California, the simulations yield an overall decline in mean annual
 269 precipitation mainly due to a notable decline in winter precipitation with only a slight increase in

270 summer (Fig. 4). This pattern is produced by both the water isotope-enabled iCESM1.2 and the
271 higher resolution CAM5 with an overall shift into lower amplitude seasonal cycles (i.e., drier
272 winter/spring and a slightly wetter summer) (Fig. 4, 5). This seasonal wet-dry shift appears to be
273 driven in part by a pronounced northward shift of atmospheric rivers (ARs) in winter along the
274 North American Pacific coastline (Shields et al., 2021). As ARs deliver most of the winter
275 precipitation to the mid-latitude Pacific coast, less frequent occurrences result in drier winters
276 during the PETM. Moreover, the extreme value index (ξ) shows a small but statistically robust
277 increase in winter (DJF) wet extremes with a significant increase in the probability of summer
278 (JJA) wet exceedance during PETM (Fig. 5b). The latter might be due to elevated tropical storm
279 activity along the Pacific coast during PETM (Fig. S7; Kiehl et al., 2021).

280 4.2 Hydroclimate response from observations.

281 4.2.1 Sedimentation rate, clay assemblages and grain size distribution

282 Arguably, the collection of observations from Lodo (i.e, sediment flux, clay assemblages, and
283 leaf wax $\delta^2\text{H}$ isotopes), within limitations, appear to be mostly consistent with the model output.
284 Starting with siliciclastic sedimentation, rates should be highly susceptible to a major shift in
285 hydrologic conditions as changes in the seasonality of precipitation (along with vegetative cover)
286 would impact rates of erosion and sediment transport. The coarse resolution of stratigraphic
287 control at Lodo does limit the ability to constrain changes in sedimentation rates in detail.
288 However, just considering the thickness of the CIE (~ 10 m), one could argue for a shift toward
289 higher seasonality of precipitation with overall drier conditions as suggested by John et al.,
290 (2008).

291
292 The other constraints on regional precipitation would also support a shift toward drier conditions.
293 For example, an increase in the relative abundance of kaolinite fluxes has been widely observed
294 across the CIE onset in many PETM sections from mid to high latitudes (Tateo, 2020; Gibson et
295 al., 2000) and interpreted as evidence of a major mode shift in local hydroclimates. In contrast,
296 the clay mineralogy (Fig. 3) for the Lodo Formation is dominated mainly by smectite at the onset
297 of the PETM, consistent with seasonal wet/dry cycles under warm conditions (Gibson et al.,
298 2000). A subtle increase in the kaolinite/smectite could be interpreted as evidence of higher

299 humidity (Gibson et al., 2000). However, the skewed grain size distribution of clay sediments
300 around 8 m coinciding with illite/smectite peaks (Fig. 3e and S1) indicate higher fluvial velocity
301 and increased erosion as observed elsewhere (Chen et al., 2018; Foreman et al., 2012; Foreman,
302 2014). For example, along the mid-Atlantic margin it appears the kaolinite might have been
303 exhumed from local Cretaceous laterites (Lyons et al., 2018). This enhanced physical weathering
304 and erosion at Lodo could be related to an increase in episodic wet/dry extremes as seasonality
305 intensified during the PETM.

306

307 4.2.2 Precipitation and Leaf wax $\delta^2\text{H}_{n\text{-alkane}}$

308 The Lodo leaf wax $\delta^2\text{H}_{n\text{-alkane}}$ record at first glance is somewhat equivocal in terms of the
309 response of local hydroclimate. In theory, terrestrial higher plant $\delta^2\text{H}_{n\text{-alkane}}$ should provide
310 insight into changes in regional precipitation amounts/source, particularly major mode shifts
311 (Handley et al., 2008, 2011; Jaramillo et al., 2010; Pagani et al., 2006; Tipple et al., 2011). In
312 some PETM records, $\delta^2\text{H}_{n\text{-alkane}}$ significantly increases, consistent with the effects of higher T on
313 water isotope fractionation. For example, in the Arctic, $\delta^2\text{H}_{n\text{-alkane}}$ records show a positive
314 excursion of 55‰ at CIE onset, consistent with higher T, a reduced meridional temperature
315 gradient and decreasing isotope distillation during vapor transport (Pagani et al., 2006).
316 However, there are notable exceptions. In some subtropical/mid-latitude sites, $\delta^2\text{H}_{n\text{-alkane}}$
317 decreases (ca ~20‰) across the onset of PETM (Handley et al., 2008, 2011; Jaramillo et al.,
318 2010; Tipple et al., 2011). In comparison, Lodo $\delta^2\text{H}_{n\text{-alkane}}$ displays a comparatively muted
319 response, showing a slight ^2H enrichment in the main body PETM followed by several
320 anomalous shifts toward more negative values (Fig. 2c).

321

322 Given the robust evidence for mode shifts in hydroclimate elsewhere during the PETM, does the
323 relatively stable Lodo $\delta^2\text{H}_{n\text{-alkane}}$ record necessarily support a local/regional stable hydroclimate
324 (i.e., in conflict with the modeling and other observations)? As H-isotope fractionation in plants
325 is related to photosynthetic pathways, source water availability, and atmospheric humidity
326 (Sachse et al., 2012; Tipple et al., 2015), it's possible that local shifts in meteoric water isotope
327 composition were offset by another influencing factor(s). Regarding photosynthetic pathways,
328 along the west coast of North America, no detailed records of vegetation response have been
329 generated for the PETM. Still, for the late Paleocene and early Eocene intervals, Korasidis et al.

330 (2022) found little deviation in the Koppen-Geiger climate type (i.e., Mediterranean) within the
331 central California region. This evidence along with the lack of change in average chain length
332 (ACL) in the Lodo section (Fig S5) would suggest no major changes in vegetation assemblages
333 during the PETM. Another factor, reworking of Paleocene terrestrial organic matter (e.g., Tipple
334 et al., 2011), could possibly dampen of isotopic n -alkane signals at Lodo, although the CPI and
335 the leaf wax carbon isotopes would suggest minimal reworking of the n -alkanes, as opposed to
336 other coastal PETM sites where the evidence for reworking is robust (e.g., Lyons et al., 2018).
337 As such, if we assume the $\delta^2\text{H}_{n\text{-alkane}}$ record reflects only on changes in local meteoric waters, the
338 observed modest change of $\delta^2\text{H}_{n\text{-alkane}}$ values at Lodo could be interpreted in several ways in
339 terms of T-related changes on isotope fractionation that were offset by changes in dominant
340 season of precipitation, and/or vapor sources and distance of transport. For example, a shift in
341 precipitation between winter and late summer/fall could offset the effects of warming assuming a
342 shift from a proximal (north or central Pacific) to a more distal (Gulf of Mexico) source of vapor
343 (Hu and Dominguez, 2015). At ground level, stronger evapo-transpiration during biosynthesis
344 can isotopically be offset by external water source availability (i.e. seasonal precipitation).
345 Local/regional ground water table variations caused by hydrological change would also affect the
346 source water-use efficiency of plants since surface water tends to be more depleted in some
347 perennial species after intense storms in the groundwater (Hou et al., 2008; Krishnan et al.,
348 2014). Hydrogen isotope fractionation in plants can also be biased by seasonal shift in regional
349 vegetation growth regime. For example, leaf wax lipids from terrestrial plants usually record
350 hydrological conditions earlier in the season rather than fully integrating the entire growing
351 season (Hou et al., 2008; Tipple et al., 2013). Finally, episodic extremes in precipitation may
352 dominate the hydrogen isotopic composition of the leaf wax (Krishnan et al., 2014). If soil water
353 is derived mainly from extreme events during the growth season, the lack of a major shift in the
354 Lodo $\delta^2\text{H}_{n\text{-alkane}}$ record with the onset of the PETM could reflect a combination of more ^2H -
355 depleted precipitation delivered by seasonal storms offset by warming induced ^2H -enrichment in
356 leaf water.

357

358 4.3 Comparison of leaf water and modeled $\delta^2\text{H}$

359 Assuming leaf wax $\delta^2\text{H}$ is primarily influenced by local meteoric water, how does the seasonal
360 distribution of precipitation influence the bulk signal? In iCESM1.2 simulations with increasing

361 $p\text{CO}_2$ (i.e., 3x to 6x pre-industry) and SST, the seasonal shifts in $\delta^2\text{H}$ of mean monthly
362 precipitation from pre-PETM to PETM is significant. During the winter, as precipitation amounts
363 decline, $\delta^2\text{H}_{\text{precip}}$ increases by 10‰ while decreasing by ~1 to 5‰ during late summer/fall in
364 central California (Fig. 4). To estimate how this seasonal change of $\delta^2\text{H}_{\text{precip}}$ and precipitation
365 amount influences leaf water $\delta^2\text{H}$, we applied a leaf wax proxy model (supplemental
366 information) which computes the combined effects of changes in seasonal precipitation and
367 growing season length. The model shows leaf water $\delta^2\text{H}$ enriched ca. 4 to 7‰ from pre-PETM to
368 PETM. Arguably, this would be consistent with minor ~6‰ enrichment observed in the Lodo
369 record at the onset of the PETM. We also examined other sites for comparison of the predicted
370 leaf water differences from pre-PETM to PETM with the fossil leaf wax $\Delta\delta^2\text{H}$ (see supplemental
371 information) and find a similar pattern in other mid-latitude sites. Therefore, this relatively
372 muted leaf wax $\delta^2\text{H}_{n\text{-alkane}}$ response can be potentially explained by a seasonal shift of heavy
373 precipitation events. Other factors to consider include precipitation source waters and a shift of a
374 mixing endmember between proximal and distal sources of water in the coast (Romero and
375 Feakins, 2011). For example, with a summer shift of source water from the Pacific to subtropics
376 (i.e., summer monsoons), the effect of increasing distance and distillation would isotopically
377 deplete vapor (Hu and Dominguez, 2015), thus offsetting the temperature related enrichment of
378 local $\delta^2\text{H}_{\text{precip}}$. In addition, infrequent but high intensity tropical cyclones during the PETM
379 (Kiehl et al., 2021) would tend to deliver relatively depleted precipitation (i.e., a more negative
380 $\delta^2\text{H}$) during summer months.

381
382 Finally, a related record that might indirectly reflect on precipitation amount (i.e., atmospheric
383 humidity) is the magnitude of the CIE as recorded by leaf wax $\delta^{13}\text{C}_{n\text{-alkane}}$. Recalcitrant higher
384 plants leaf wax n -alkane carbon isotope ratios ($n>25$ with odd-over-even preference) reflect
385 mainly carbon source (Diefendorf et al., 2010). However, photosynthetic carbon isotope
386 fractionation (Δ_p) is sensitive to atmospheric $p\text{CO}_2$ variations, generally increase with rising
387 concentrations assuming a constant photosynthetic fractionation factor and humidity (Diefendorf
388 et al., 2010). The $\delta^{13}\text{C}_{n\text{-alkane}}$ of Lodo section displays a sharp negative shift of ca. 4 ‰ (average
389 of $n\text{-C}_{27}$, $n\text{-C}_{29}$, $n\text{-C}_{31}$) across the onset of CIE (Fig. 2b), which is consistent with global mean
390 atmospheric CIE (Sluijs and Dickens, 2012) but generally smaller than observed in other leaf
391 wax records (Handley et al., 2008, 2011; Jaramillo et al., 2010; Pagani et al., 2006; Tipple et al.,

392 2011). The smaller $\delta^{13}\text{C}_{n\text{-alkane}}$ CIE recorded in Lodo could reflect on reduction in local humidity
393 which preferentially tends to reduce the magnitude of Δ_p during photosynthetic carbon fixation.

394

395 Summary and Conclusions

396

397 Many sections globally exhibit evidence, often striking, of significant shifts in local hydroclimate
398 at the onset of the PETM consistent with model simulations (e.g., 2x CO₂). These same models
399 also simulate an overall decrease in winter precipitation for the central California coast due in
400 large part to a reduction in AR frequency (Shields et al., 2021). While not as striking, the
401 collection of observations from the central California Lodo Gulch Section would support a
402 modest reduction in precipitation (i.e. MAP) during the PETM along with the possibility of an
403 increase in the frequency of extreme precipitation events. This transition toward greater aridity
404 and precipitation extremes is not unlike the forecasts for much of California over the coming
405 centuries due to anthropogenic warming.

406

407

408 Data availability. Data tables of clay assemblages, grain size, organic carbon isotopes and leaf
409 wax *n*-alkane stable isotopes will be available via the PANGAEA repository..

410

411 Author contribution. JCZ conceived the project design, acquired funding and provided overall
412 supervision. XZ conducted stable isotope measurements, clay mineralogy, grain size analyses
413 and iCESM/CAM5 model output analyses. Leaf wax *n*-alkane carbon and hydrogen isotope
414 measurements were performed by BJT. JBN conducted leaf wax proxy model experiments. CAS
415 and WDR contributed to processing CAM model output. This paper was prepared by XZ with all
416 authors contribution to the review and editing of the manuscript.

417

418 Competing interests. The authors declare that they have no conflict of interest.

419

420 Acknowledgements.

421 We thank Colin Carney (UCSC SIL) for technical support and acknowledge the contributions of
422 Dr. Mark Pagani (deceased). Funding for this project has been provided by National Science
423 Foundation No. OCE 2103513 to JCZ. All compound specific isotope analyses were performed
424 at the Yale Institute for Biospheric Studies-Earth Systems Center that was supported by National
425 Science Foundation Grant EAR 0628358 and OCE 0902993. The CESM project is supported
426 primarily by the National Science Foundation (NSF). This material is based upon work

427 supported by the National Center for Atmospheric Research, which is a major facility sponsored
428 by the NSF under Cooperative Agreement No. 1852977.

429

430 References:

- 431 Abell, J. T., Winckler, G., Anderson, R. F., and Herbert, T. D.: Poleward and weakened westerlies
432 during Pliocene warmth, *Nature*, 589, 70–75, <https://doi.org/10.1038/s41586-020-03062-1>, 2021.
- 433 Blott, S. J., Croft, D. J., Pye, K., Saye, S. E., & Wilson, H. E. Particle size analysis by laser
434 diffraction. Geological Society, London, Special Publications, 232(1), 63-73, 2004.
- 435 Brabb, E. E.: Studies in Tertiary stratigraphy of the California Coast Ranges., US Geological
436 Survey Professional Paper, 1213, 1983.
- 437 Brady, E., Stevenson, S., Bailey, D., Liu, Z., Noone, D., Nusbaumer, J., Otto-Bliesner, B. L., Tabor,
438 C., Tomas, R., Wong, T., Zhang, J., and Zhu, J.: The Connected Isotopic Water Cycle in the
439 Community Earth System Model Version 1, *J Adv Model Earth Syst*, 11, 2547–2566,
440 <https://doi.org/10.1029/2019MS001663>, 2019.
- 441 Büntgen, U., Urban, O., Krusic, P. J., Rybníček, M., Kolář, T., Kyncl, T., Ač, A., Koňasová, E.,
442 Čáslavský, J., Esper, J., Wagner, S., Saurer, M., Tegel, W., Dobrovolný, P., Cherubini, P.,
443 Reinig, F., and Trnka, M.: Recent European drought extremes beyond Common Era background
444 variability, *Nat Geosci*, 14, 190–196, <https://doi.org/10.1038/s41561-021-00698-0>, 2021.
- 445 Campbell, J., Poulsen, C. J., Zhu, J., Tierney, J. E., and Keeler, J.: CO₂-driven and orbitally driven
446 oxygen isotope variability in the Early Eocene, *Clim. Past*, 20, 495–522,
447 <https://doi.org/10.5194/cp-20-495-2024>, 2024.
- 448 Carmichael, M. J., Lunt, D. J., Huber, M., Heinemann, M., Kiehl, J., LeGrande, A., Loptson, C. A.,
449 Roberts, C. D., Sagoo, N., Shields, C., Valdes, P. J., Winguth, A., Winguth, C., and Pancost, R.
450 D.: A model-model and data-model comparison for the early Eocene hydrological cycle, *Climate*
451 *of the Past*, 12, 455–481, <https://doi.org/10.5194/CP-12-455-2016>, 2016.
- 452 Carmichael, M. J., Inglis, G. N., Badger, M. P. S., Naafs, B. D. A., Behrooz, L., Remmelzwaal, S.,
453 Monteiro, F. M., Rohrssen, M., Farnsworth, A., Buss, H. L., Dickson, A. J., Valdes, P. J., Lunt,
454 D. J., and Pancost, R. D.: Hydrological and associated biogeochemical consequences of rapid
455 global warming during the Paleocene-Eocene Thermal Maximum,
456 <https://doi.org/10.1016/j.gloplacha.2017.07.014>, 1 October 2017.
- 457 Cramwinckel, M. J., Burls, N. J., Fahad, A. A., Knapp, S., West, C. K., Reichgelt, T., ... & Inglis,
458 G. N. Global and zonal-mean hydrological response to early Eocene warmth. *Paleoceanography*
459 *and Paleoclimatology*, 38(6), e2022PA004542, 2023.
- 460 Chen, C., Guerit, L., Foreman, B. Z., Hassenruck-Gudipati, H. J., Adatte, T., Honegger, L., Perret,
461 M., Sluijs, A., and Castellort, S.: Estimating regional flood discharge during Palaeocene-Eocene
462 global warming, *Sci Rep*, 8, 1–8, <https://doi.org/10.1038/s41598-018-31076-3>, 2018.
- 463 Diefendorf, A. F., Mueller, K. E., Wing, S. L., Koch, P. L., and Freeman, K. H.: Global patterns in
464 leaf ¹³C discrimination and implications for studies of past and future climate, *Proc Natl Acad*
465 *Sci U S A*, 107, 5738–5743, <https://doi.org/10.1073/pnas.0910513107>, 2010.
- 466 Douville, H., Raghavan, K., Renwick, J., and Allan, R.: Water Cycle Changes, Intergovernmental
467 Panel on Climate Change 2021 – The Physical Science Basis, 1055–1210,
468 <https://doi.org/10.1017/9781009157896.010>, 2021.

469 Foreman, B. Z.: Climate-driven generation of a fluvial sheet sand body at the Paleocene–Eocene
470 boundary in north-west Wyoming (USA), *Basin Research*, 26, 225–241,
471 <https://doi.org/10.1111/BRE.12027>, 2014.

472 Foreman, B. Z., Heller, P. L., and Clementz, M. T.: Fluvial response to abrupt global warming at
473 the Palaeocene/Eocene boundary, *Nature* 2012 491:7422, 491, 92–95,
474 <https://doi.org/10.1038/nature11513>, 2012.

475 Gibson, T. G., Bybell, L. M., and Mason, D. B.: Stratigraphic and climatic implications of clay
476 mineral changes around the Paleocene/Eocene boundary of the northeastern US margin,
477 *Sediment Geol*, 134, 65–92, [https://doi.org/10.1016/S0037-0738\(00\)00014-2](https://doi.org/10.1016/S0037-0738(00)00014-2), 2000.

478 Handley, L., Pearson, P. N., McMillan, I. K., and Pancost, R. D.: Large terrestrial and marine
479 carbon and hydrogen isotope excursions in a new Paleocene/Eocene boundary section from
480 Tanzania, *Earth Planet Sci Lett*, 275, 17–25, <https://doi.org/10.1016/j.epsl.2008.07.030>, 2008.

481 Handley, L., Crouch, E. M., and Pancost, R. D.: A New Zealand record of sea level rise and
482 environmental change during the Paleocene-Eocene Thermal Maximum, *Palaeogeogr*
483 *Palaeoclimatol Palaeoecol*, 305, 185–200, <https://doi.org/10.1016/j.palaeo.2011.03.001>, 2011.

484 Handley, L., O’Halloran, A., Pearson, P. N., Hawkins, E., Nicholas, C. J., Schouten, S., McMillan,
485 I. K., and Pancost, R. D.: Changes in the hydrological cycle in tropical East Africa during the
486 Paleocene-Eocene Thermal Maximum, *Palaeogeogr Palaeoclimatol Palaeoecol*, 329–330, 10–21,
487 <https://doi.org/10.1016/j.palaeo.2012.02.002>, 2012.

488 Held, I. M. and Soden, B. J.: Robust Responses of the Hydrological Cycle to Global Warming, *J*
489 *Clim*, 19, 5686–5699, <https://doi.org/10.1175/JCLI3990.1>, 2006.

490 Hou, J., D’Andrea, W. J., and Huang, Y.: Can sedimentary leaf waxes record D/H ratios of
491 continental precipitation? Field, model, and experimental assessments, *Geochim Cosmochim*
492 *Acta*, 72, 3503–3517, <https://doi.org/10.1016/j.gca.2008.04.030>, 2008.

493 Hu, H. and Dominguez, F.: Evaluation of Oceanic and Terrestrial Sources of Moisture for the North
494 American Monsoon Using Numerical Models and Precipitation Stable Isotopes, *J*
495 *Hydrometeorol*, 16, 19–35, <https://doi.org/10.1175/JHM-D-14-0073.1>, 2015.

496 Jaramillo, C., Ochoa, D., Contreras, L., Pagani, M., Carvajal-Ortiz, H., Pratt, L. M., Krishnan, S.,
497 Cardona, A., Romero, M., Quiroz, L., Rodriguez, G., Rueda, M. J., De La Parra, F., Morón, S.,
498 Green, W., Bayona, G., Montes, C., Quintero, O., Ramirez, R., Mora, G., Schouten, S.,
499 Bermudez, H., Navarrete, R., Parra, F., Alvarán, M., Osorno, J., Crowley, J. L., Valencia, V., and
500 Vervoort, J.: Effects of rapid global warming at the paleocene-eocene boundary on neotropical
501 vegetation, *Science* (1979), 330, 957–961, <https://doi.org/10.1126/science.1193833>, 2010.

502 John, C. M., Bohaty, S. M., Zachos, J. C., Sluijs, A., Gibbs, S., Brinkhuis, H., and Bralower, T. J.:
503 North American continental margin records of the Paleocene–Eocene thermal maximum:
504 Implications for global carbon and hydrological cycling, *Paleoceanography*, 23,
505 <https://doi.org/10.1029/2007PA001465>, 2008.

506 Kemp, S. J., Ellis, M. A., Mountney, I., and Kender, S.: Palaeoclimatic implications of high-
507 resolution clay mineral assemblages preceding and across the onset of the Palaeocene–Eocene
508 Thermal Maximum, North Sea Basin, *Clay Miner*, 51, 793–813,
509 <https://doi.org/10.1180/CLAYMIN.2016.051.5.08>, 2016.

510 Kiehl, J. T. and Shields, C. A.: Sensitivity of the palaeocene-eocene thermal maximum climate to
511 cloud properties, *Philosophical Transactions of the Royal Society A: Mathematical, Physical and*
512 *Engineering Sciences*, 371, <https://doi.org/10.1098/rsta.2013.0093>, 2013.

513 Kiehl, J. T., Shields, C. A., Snyder, M. A., Zachos, J. C., and Rothstein, M.: Greenhouse- and
514 orbital-forced climate extremes during the early Eocene, *Philosophical Transactions of the Royal*

515 Society A: Mathematical, Physical and Engineering Sciences, 376,
516 <https://doi.org/10.1098/RSTA.2017.0085>, 2018.

517 Kiehl, J. T., Zarzycki, C. M., Shields, C. A., and Rothstein, M. V.: Simulated changes to tropical
518 cyclones across the Paleocene-Eocene Thermal Maximum (PETM) boundary, *Palaeogeogr*
519 *Palaeoclimatol Palaeoecol*, 572, 110421, <https://doi.org/10.1016/J.PALAEO.2021.110421>, 2021.

520 Korasidis, V. A., Wing, S. L., Shields, C. A., and Kiehl, J. T.: Global Changes in Terrestrial
521 Vegetation and Continental Climate During the Paleocene-Eocene Thermal Maximum,
522 *Paleoceanogr Paleoclimatol*, 37, <https://doi.org/10.1029/2021PA004325>, 2022.

523 Kozdon, R., Penman, D. E., Kelly, D. C., Zachos, J. C., Fournelle, J. H., and Valley, J. W.:
524 Enhanced Poleward Flux of Atmospheric Moisture to the Weddell Sea Region (ODP Site 690)
525 During the Paleocene-Eocene Thermal Maximum, *Paleoceanogr Paleoclimatol*, 35, 1–14,
526 <https://doi.org/10.1029/2019pa003811>, 2020.

527 Kraus, M. J. and Riggins, S.: Transient drying during the Paleocene-Eocene Thermal Maximum
528 (PETM): Analysis of paleosols in the bighorn basin, Wyoming, *Palaeogeogr Palaeoclimatol*
529 *Palaeoecol*, 245, 444–461, <https://doi.org/10.1016/j.palaeo.2006.09.011>, 2007.

530 Krishnan, S., Pagani, M., Huber, M., and Sluijs, A.: High latitude hydrological changes during the
531 Eocene Thermal Maximum 2, *Earth Planet Sci Lett*, 404, 167–177,
532 <https://doi.org/10.1016/j.epsl.2014.07.029>, 2014.

533 Liu, B., Yan, Y., Zhu, C., Ma, S., and Li, J.: Record-Breaking Meiyu Rainfall Around the Yangtze
534 River in 2020 Regulated by the Subseasonal Phase Transition of the North Atlantic Oscillation,
535 *Geophys Res Lett*, 47, <https://doi.org/10.1029/2020GL090342>, 2020.

536 Massoud, E. C., Espinoza, V., Guan, B., and Waliser, D. E.: Global Climate Model Ensemble
537 Approaches for Future Projections of Atmospheric Rivers, *Earths Future*, 7, 1136–1151,
538 <https://doi.org/10.1029/2019EF001249>, 2019.

539 McInerney, F. A. and Wing, S. L.: The Paleocene-Eocene Thermal Maximum: A Perturbation of
540 Carbon Cycle, Climate, and Biosphere with Implications for the Future, *Annu Rev Earth Planet*
541 *Sci*, 39, 489–516, <https://doi.org/10.1146/annurev-earth-040610-133431>, 2011.

542 Nicolo, M. J., Dickens, G. R., and Hollis, C. J.: South Pacific intermediate water oxygen depletion
543 at the onset of the Paleocene-Eocene thermal maximum as depicted in New Zealand margin
544 sections, *Paleoceanography*, 25, 1–12, <https://doi.org/10.1029/2009PA001904>, 2010.

545 Pagani, M., Pedentchouk, N., Huber, M., Sluijs, A., Schouten, S., Brinkhuis, H., Damsté, J. S. S.,
546 Dickens, G. R., Backman, J., Clemens, S., Cronin, T., Eynaud, F., Gattacceca, J., Jakobsson, M.,
547 Jordan, R., Kaminski, M., King, J., Koc, N., Martinez, N. C., McInroy, D., Moore, T. C.,
548 O'Regan, M., Onodera, J., Pälike, H., Rea, B., Rio, D., Sakamoto, T., Smith, D. C., St John, K.
549 E. K., Suto, I., Suzuki, N., Takahashi, K., Watanabe, M., and Yamamoto, M.: Arctic hydrology
550 during global warming at the Palaeocene/Eocene thermal maximum, *Nature*, 442, 671–675,
551 <https://doi.org/10.1038/nature05043>, 2006.

552 Peters, K.E., Walters, C.C., Moldowan, J.M., 2005. *The Biomarker Guide: II Biomarkers*
553 *and Isotopes in Petroleum Systems and Earth History*, 2nd edition. Cambridge Uni-
554 *versity Press, Cambridge.*

555 Risser, M. D. and Wehner, M. F.: Attributable Human-Induced Changes in the Likelihood and
556 Magnitude of the Observed Extreme Precipitation during Hurricane Harvey, *Geophys Res Lett*,
557 44, 12,457–12,464, <https://doi.org/10.1002/2017GL075888>, 2017.

558 Romero, I. C. and Feakins, S. J.: Spatial gradients in plant leaf wax D/H across a coastal salt marsh
559 in southern California, *Org Geochem*, 42, 618–629,
560 <https://doi.org/10.1016/J.ORGGEOCHEM.2011.04.001>, 2011.

561 Rush, W. D., Kiehl, J. T., Shields, C. A., and Zachos, J. C.: Increased frequency of extreme
562 precipitation events in the North Atlantic during the PETM: Observations and theory,
563 *Palaeogeogr Palaeoclimatol Palaeoecol*, 568, <https://doi.org/10.1016/j.palaeo.2021.110289>,
564 2021.

565 Sachse, D., Billault, I., Bowen, G. J., Chikaraishi, Y., Dawson, T. E., Feakins, S. J., Freeman, K. H.,
566 Magill, C. R., McInerney, F. A., van der Meer, M. T. J., Polissar, P., Robins, R. J., Sachs, J. P.,
567 Schmidt, H.-L., Sessions, A. L., White, J. W. C., West, J. B., and Kahmen, A.: Molecular
568 Paleohydrology: Interpreting the Hydrogen-Isotopic Composition of Lipid Biomarkers from
569 Photosynthesizing Organisms, *Annu Rev Earth Planet Sci*, 40, 221–249,
570 <https://doi.org/10.1146/annurev-earth-042711-105535>, 2012.

571 Schmitz, B. and Pujalte, V.: Sea-level, humidity, and land-erosion records across the initial Eocene
572 thermal maximum from a continental-marine transect in northern Spain, *Geology*, 31, 689–692,
573 <https://doi.org/10.1130/G19527.1>, 2003.

574 Self-Trail, J. M., Robinson, M. M., Bralower, T. J., Sessa, J. A., Hajek, E. A., Kump, L. R.,
575 Trampush, S. M., Willard, D. A., Edwards, L. E., Powars, D. S., and Wandless, G. A.: Shallow
576 marine response to global climate change during the Paleocene-Eocene Thermal Maximum,
577 Salisbury Embayment, USA, *Paleoceanography*, 32, 710–728,
578 <https://doi.org/10.1002/2017PA003096>, 2017.

579 Shields, C. A. and Kiehl, J. T.: Atmospheric river landfall-latitude changes in future climate
580 simulations, *Geophys Res Lett*, 43, 8775–8782, <https://doi.org/10.1002/2016GL070470>, 2016.

581 Shields, C. A., Kiehl, J. T., Rush, W., Rothstein, M., and Snyder, M. A.: Atmospheric rivers in
582 high-resolution simulations of the Paleocene Eocene Thermal Maximum (PETM), *Palaeogeogr*
583 *Palaeoclimatol Palaeoecol*, 567, <https://doi.org/10.1016/j.palaeo.2021.110293>, 2021.

584 Simon Wang, S. Y., Yoon, J. H., Becker, E., and Gillies, R.: California from drought to deluge,
585 *Nature Climate Change* 2017 7:7, 7, 465–468, <https://doi.org/10.1038/nclimate3330>, 2017.

586 Slotnick, B. S., Dickens, G. R., Nicolo, M. J., Hollis, C. J., Crampton, J. S., Zachos, J. C., and
587 Sluijs, A.: Large-amplitude variations in carbon cycling and terrestrial weathering during the
588 latest Paleocene and earliest Eocene: The record at Mead Stream, New Zealand, *Journal of*
589 *Geology*, 120, 487–505, <https://doi.org/10.1086/666743>, 2012.

590 Sluijs, A. and Brinkhuis, H.: A dynamic climate and ecosystem state during the Paleocene-Eocene
591 Thermal Maximum: Inferences from dinoflagellate cyst assemblages on the New Jersey Shelf,
592 *Biogeosciences*, 6, 1755–1781, <https://doi.org/10.5194/bg-6-1755-2009>, 2009.

593 Sluijs, A. and Dickens, G. R.: Assessing offsets between the $\delta^{13}\text{C}$ of sedimentary components and
594 the global exogenic carbon pool across early Paleogene carbon cycle perturbations, *Global*
595 *Biogeochem Cycles*, 26, <https://doi.org/10.1029/2011GB004224>, 2012.

596 Sluijs, A., Brinkhuis, H., Crouch, E. M., John, C. M., Handley, L., Munsterman, D., Bohaty, S. M.,
597 Zachos, J. C., Reichert, G. J., Schouten, S., Pancost, R. D., Damsté, J. S. S., Welters, N. L. D.,
598 Lotter, A. F., and Dickens, G. R.: Eustatic variations during the Paleocene-Eocene greenhouse
599 world, *Paleoceanography*, 23, <https://doi.org/10.1029/2008PA001615>, 2008.

600 Smith, F. A., Wing, S. L., and Freeman, K. H.: Magnitude of the carbon isotope excursion at the
601 Paleocene-Eocene thermal maximum: The role of plant community change, *Earth Planet Sci*
602 *Lett*, 262, 50–65, <https://doi.org/10.1016/j.epsl.2007.07.021>, 2007.

603 Stassen, P., Thomas, E., and Speijer, R. P.: The progression of environmental changes during the
604 onset of the Paleocene-Eocene thermal maximum (New Jersey coastal plain), *Austrian Journal of*
605 *Earth Sciences*, 105, 169–178, 2012.

606 Stevenson, S., Coats, S., Touma, D., Cole, J., Lehner, F., Fasullo, J., and Otto-Bliesner, B.: Twenty-
607 first century hydroclimate: A continually changing baseline, with more frequent extremes,
608 PNAS, 119, <https://doi.org/10.1073/pnas>, 2022.

609 Swain, D. L., Langenbrunner, B., Neelin, J. D., and Hall, A.: Increasing precipitation volatility in
610 twenty-first-century California, *Nat Clim Chang*, 8, 427–433, <https://doi.org/10.1038/s41558-018-0140-y>, 2018.

612 Tateo, F.: Clay minerals at the paleocene–eocene thermal maximum: Interpretations, limits, and
613 perspectives, *Minerals*, 10, 1–16, <https://doi.org/10.3390/min10121073>, 2020.

614 Tipple, B. J., Pagani, M., Krishnan, S., Dirghangi, S. S., Galeotti, S., Agnini, C., Giusberti, L., and
615 Rio, D.: Coupled high-resolution marine and terrestrial records of carbon and hydrologic cycles
616 variations during the Paleocene – Eocene Thermal Maximum (PETM), *Earth Planet Sci Lett*,
617 311, 82–92, <https://doi.org/10.1016/j.epsl.2011.08.045>, 2011.

618 Tipple, B. J., Berke, M. A., Doman, C. E., Khachatryan, S., and Ehleringer, J. R.: Leaf-wax n-
619 alkanes record the plant-water environment at leaf flush, *Proc Natl Acad Sci U S A*, 110, 2659–
620 2664, <https://doi.org/10.1073/pnas.1213875110>, 2013.

621 Tipple, B. J., Berke, M. A., Hambach, B., Roden, J. S., and Ehleringer, J. R.: Predicting leaf wax n-
622 alkane 2H/1H ratios: controlled water source and humidity experiments with hydroponically
623 grown trees confirm predictions of Craig–Gordon model, *Plant Cell Environ*, 38, 1035–1047,
624 <https://doi.org/10.1111/PCE.12457>, 2015.

625 Vogel, M. M., Hauser, M., and Seneviratne, S. I.: Projected changes in hot, dry and wet extreme
626 events’ clusters in CMIP6 multi-model ensemble, *Environmental Research Letters*, 15,
627 <https://doi.org/10.1088/1748-9326/ab90a7>, 2020.

628 Wakeham, S. G. and Pease, T. K.: *Lipid Analysis in Marine Particle and Sediment Samples A*
629 *Laboratory Handbook*, 2004.

630 Williams, A. P., Cook, E. R., Smerdon, J. E., Cook, B. I., Abatzoglou, J. T., Bolles, K., Baek, S. H.,
631 Badger, A. M., and Livneh, B.: Large contribution from anthropogenic warming to an emerging
632 North American megadrought, *Science* (1979), 368, 314–318, 2020.

633 Willis, K.J, McElwain, J. C.: *The Evolution of Plants*, OUP Oxford, 392 pp., 2002.

634 Wing, S. L., Harrington, G. J., Smith, F. a, Bloch, J. I., Boyer, D. M., and Freeman, K. H.: Transient
635 Floral Change and rapid global warming at the P/E boundary, *Science* (1979), 310, 993–996,
636 <https://doi.org/10.1126/science.1116913>, 2005.

637 Zachos, J. C., Dickens, G. R., and Zeebe, R. E.: An early Cenozoic perspective on greenhouse
638 warming and carbon-cycle dynamics, *Nature*, 451, 279–283,
639 <https://doi.org/10.1038/nature06588>, 2008.

640 Zhu, J., Poulsen, C. J., Otto-Bliesner, B. L., Liu, Z., Brady, E. C., and Noone, D. C.: Simulation of
641 early Eocene water isotopes using an Earth system model and its implication for past climate
642 reconstruction, *Earth Planet Sci Lett*, 537, 116164, <https://doi.org/10.1016/j.epsl.2020.116164>,
643 2020.

644 Zscheischler, J. and Lehner, F.: *Attributing Compound Events to Anthropogenic Climate Change*,
645 *Bull Am Meteorol Soc*, 103, E936–E953, <https://doi.org/10.1175/BAMS-D-21-0116.1>, 2022.

646